ChemPubSoc Europe

DOI: 10.1002/chem.201604065

CHEMISTRY A European Journal Full Paper

Perovskite Oxide Catalysis

# Defect Engineering, Electronic Structure, and Catalytic Properties of Perovskite Oxide $La_{0.5}Sr_{0.5}CoO_{3-\delta}$

Xiyang Wang, Keke Huang, Wei Ma, Yingge Cong, Chengda Ge, and Shouhua Feng*[a]

**Abstract:** The electronic structures of transition metal oxides play a crucial role in the physical and chemical properties of solid materials. Defect engineering is an efficient way to regulate the electronic structure and improve the performance of materials. Here, we develop a defect engineering route that is implemented by controlling the topochemical reactions between cobalt perovskite and urea to optimize the electronic structure of $La_{0.5}Sr_{0.5}CoO_{3-\delta}$ (LSCO). Urea pyrolysis is able to increase the oxygen defect concentration and cause octahedral distortions. Furthermore, we can distinctly observe that the introduction of oxygen vacancies narrows the hybridization orbital between O 2p and Co 3d and optimizes the O p-band center near the Fermi level by X-ray absorption spectroscopy, which greatly improves the catalytic activity of CO oxidation and photocatalytic water splitting. These results highlight the relationship between oxygen defects, electronic structure, and catalytic activity of perovskite LSCO, and demonstrate a rational approach to defect design and reveal the importance of anion redox chemistry for the structures and properties of perovskite oxides.

## Introduction

With the growing global environmental contamination and energy crisis, the study of carbon monoxide oxidation[1] and photoinduced water splitting[2] is vital to environmental management and renewable energy exploitation.[3,4] At present, precious metals have been widely studied owing to their high catalytic activity, however, the high cost and scarcity of precious metals limit their commercial application. It is extremely urgent to develop highly active and cost-effective catalysts. Perovskite oxides have great potential for CO oxidation and photoinduced water splitting because of their high catalytic activity, low cost, wide element variety, and environmental friendliness.[5] Traditional methods for improving the catalytic activity of perovskite oxides mainly focus on the specific surface area and the effect of the A cation and B cation. However, defect engineering is also viewed as one of the most effective and efficient ways to control the electronic structure of solid materials, resulting in excellent physicochemical properties.[6] Perovskite oxides generally have A-site defects and oxygen defects. In our previous work,[7] $La_{0.5}Sr_{0.5}MnO_3$ treated with dilute $HNO_3$ produced A-site defects and exposed more B-sites on the perovskite surface, which clearly improved CO catalytic activity. However, oxygen defects also have an important effect on material performance. Generally speaking, we intuitively think that transition metal (TM) cations may be the redox partner to molecular oxygen in transition metal oxides on account of the valence change of the TM cations.[8] But some recent studies indicated that surface oxygen anions of perovskite oxides acting as redox-active sites are also important to its chemical properties,[9] and the evidence reveals that the conventional surface redox center of cations is not sufficient to explain the catalytic behavior of perovskites.[1a,8c,10] Shao-Horn and co-workers have studied in depth the effect of the O p-band center position relative to the Fermi level and hybridization of the metal 3d and O 2p on the oxygen evolution reaction (OER) and the oxygen reduction reaction (ORR) of perovskite oxides by changing cations.[11] In view of this, our study addresses the effect of oxygen defects on the electronic structure and catalytic properties of perovskite oxides. The extra oxygen defects in perovskite oxides, such as $Pr_{0.5}Ba_{0.5}CoO_3$, $Sr_2CoMoO_6$, and $ACoO_3$, are usually obtained by annealing in a reducing atmosphere. However, different from these examples, LSCO ($La_{0.5}Sr_{0.5}CoO_{3-\delta}$) has a strong redox property and narrow control range. Therefore, it is very difficult for LSCO to be used to explore appropriate $H_2$ annealing temperatures and times to obtain the desired defect structures. To overcome this problem, we design a topochemical solid-state reaction between urea and perovskite LSCO to substitute $H_2$ annealing and we can control the oxygen defect concentration well by adjusting the mass ratio of LSCO and urea.

In this work, we developed a very practical method to control the oxygen defects and study in depth the correlation between oxygen defects, electronic structure, and catalytic activity such as CO oxidation and photocatalytic water splitting. Our work demonstrated that our defect engineering project is very efficient and low cost. This study also provides insights into the importance of anion redox chemistry in oxygen-deficient perovskite oxides for carbon monoxide oxidation and water

[a] X. Wang, K. Huang, W. Ma, Y. Cong, C. Ge, Prof. S. Feng
State Key Laboratory of Inorganic Synthesis and Preparative Chemistry
College of Chemistry, Jilin University Changchun 130012 (P.R. China)
Fax: (+86) 431-85168624
E-mail: shfeng@jlu.edu.cn

Supporting information for this article can be found under http://dx.doi.org/10.1002/chem.201604065.

oxidation. It will bring new opportunities to preparation of high-efficiency solid materials.

## Result and DiscussionDefect engineering of perovskite oxide $La_{0.5}Sr_{0.5}CoO_{3-\delta}$

In previous studies,[12] extra oxygen vacancies were generally obtained by annealing at high temperature in a reducing atmosphere. However, oxygen defects in perovskite LSCO is difficult to control owing to its strong redox property. In our work, we utilize solid topochemical reactions to manufacture more oxygen defects and regulate the concentration of oxygen vacancies and octahedral distortions by adjusting the mass ratio of LSCO and urea. The principle diagram of the approach to prepare oxygen-deficient perovskite LSCO is shown in Figure 1 (a). Urea, as reductant, is used to manufacture oxygen defects and oxygen in the air is used to prevent excessive reduction of perovskite. Thus, we can reasonably control its defect structure by regulating the topochemical reaction. To better clarify the chemical reaction process, we performed in situ thermogravimetric/differential thermogravimetric analysis (TG-DTA) measurements, the results of which are shown in Figure 1 (b). TG-DTA data for urea pyrolysis under an air atmosphere and pyrolysis of perovskite oxide and urea under a nitrogen atmosphere are considered as correlative data to analyze the reaction process (details in Figures S1 and S2 in the Supporting Information). Perovskite oxide is usually stable in air under 1200 K, so we clearly see that the prepared original sample (LSCO-1) basically has no weight loss or has a very small amount of weight loss and there is no endothermic and exothermic reaction with the increase in temperature. However, the measurement results of LSCO-2 and LSCO-3 show apparent changes in contrast to LSCO-1. LSCO-2 and LSCO-3 have endothermic peaks at approximately 133 °C, which are attributed to the melting of urea, and the mass loss is very small before the melting point. There is an endothermic peak at approximately 170 °C and the mass loss rate dramatically increased between 150 °C and 290 °C, which usually implies evaporation and decomposition of urea. These are consistent to TG-DTA data of urea in air (TG-DTA data of urea in air is given in the Supporting Information Figure S1).[13] However, the mass loss rate is different from that of urea between 290 °C and 460 °C, where the weight loss curves of LSCO-2 and LSCO-3 become flatter than that of urea. The DTA curve of urea has a clear endothermic peak at approximately 380 °C, where urea is further decomposed, whereas the LSCO and urea derivatives are stable coexisting compounds. The decomposition process of urea is very complicated and is all endothermic; there are many intermediate products such as ammelide, ammonium cyanate, cyanuric acid, cyanic acid, and melamine.[14] However, LSCO-3 has a noticeable exothermic peak and weight loss at approximately 520 °C, where LSCO reacts with urea derivatives and this exothermic reaction is deemed to show that LSCO produced more oxygen vacancies and its octahedral structure has serious distortion.[15] LSCO-2 does not have a sharp exothermic peak because the content of urea is relatively small. Urea derivatives and LSCO are completely pyrolyzed at approximately 650 °C, so we calcined the mixture samples for 1 h at 550–650 °C in air.

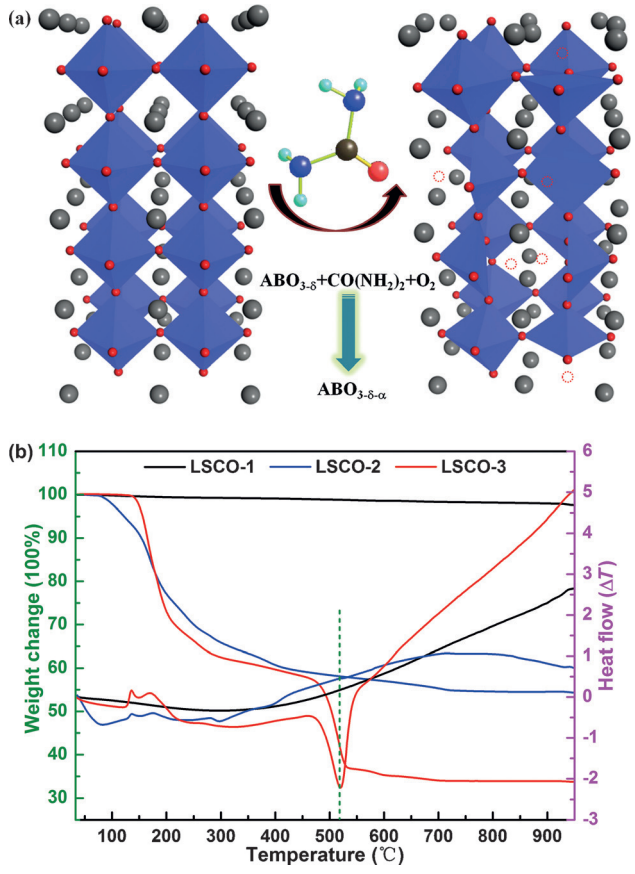


**Figure 1.** (a) The approach to prepare oxygen-deficient perovskite LSCO; the red spheres represent oxygen atoms; gray spheres represent La/Sr atoms; white spheres with red dotted lines represent oxygen vacancies. (b) TG-DTA analysis of the LSCO (1, 2, and 3) under air atmosphere; the black line (LSCO-1) indicates the original synthetic sample (LSCO) without urea; the blue line (LSCO-2) indicates the sample with LSCO/urea 5:1; the red line (LSCO-3) indicates the sample with LSCO/urea 1:2.

## Analysis of structure and oxygen defects for perovskite oxide $La_{0.5}Sr_{0.5}CoO_{3-\delta}$

Figure 2 (a) displays the XRD patterns of LSCO-1, LSCO-2, and LSCO-3, which correspond to the cubic perovskite structure (Cubic, *Pm*3*m*). All the diffraction planes are labeled in Figure 2 (a). When the ratio of urea and perovskite LSCO was gradually raised, the oxygen defects also markedly increased. The oxygen vacancy $\delta$ value in $La_{0.5}Sr_{0.5}CoO_{3-\delta}$ was determined by chemical titration. The chemical composition of the original sample LSCO-1 is $La_{0.5}Sr_{0.5}CoO_{2.87}$, that of LSCO-2 (LSCO/urea 5:1) is $La_{0.5}Sr_{0.5}CoO_{2.84}$, and that of LSCO-3 (LSCO/urea 1:2) is $La_{0.5}Sr_{0.5}CoO_{2.76}$. Meanwhile, splitting of the peak (220) of LSCO-3 around 69° was distinctly observed compared with LSCO-1 and LSCO-2 in Figure 2 (b), implying an increase in $CoO_5$ square pyramids as a result of the urea pyrolysis reaction, which coincided with the amount of oxygen vacancies measured by chemical titration.[12a] The formation of more $Co^{3+}$ with larger radius (ionic radius: $Co^{3+}$ (HS) = 0.610 Å, $Co^{3+}$

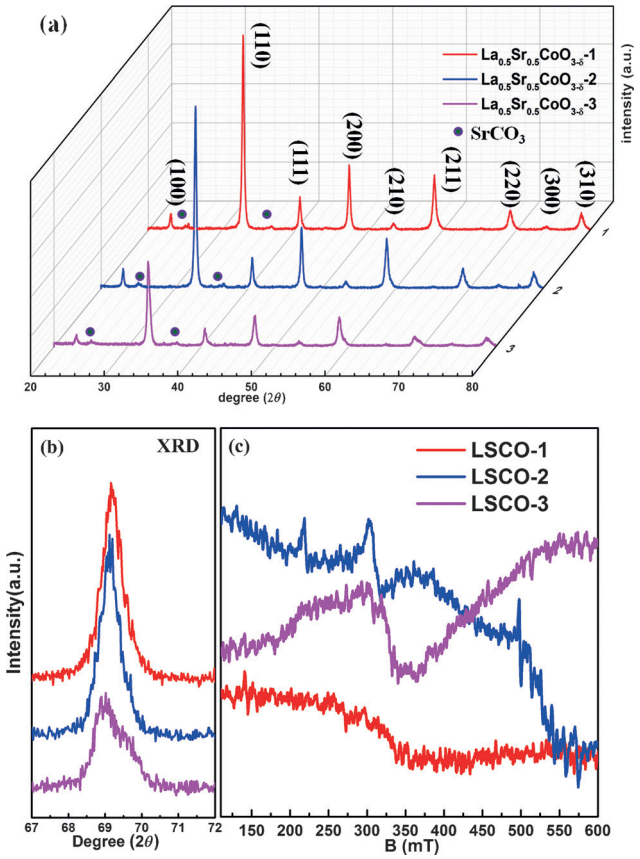


**Figure 2.** (a) X-ray diffraction (XRD) patterns of the LSCO (1, 2, and 3); the tiny peak denoted by the purple circle indicates a $SrCO_3$ secondary phase. (b) XRD patterns of the LSCO (1, 2, and 3) for (220), partially enlarged view. (c) Room-temperature ESR spectra of the LSCO (1, 2, and 3) under air atmosphere; the red line (LSCO-1) indicates the original sample (LSCO); the blue line (LSCO-2) indicates the sample with LSCO/urea 5:1; the magenta line (LSCO-3) indicates the sample with LSCO/urea 1:2.

(LS) = 0.545 Å $Co^{4+}$ = 0.530 Å) makes its lattice parameters increase, hence most peaks shifted slightly to lower angles (Figure S3(a), (b), and (c) in the Supporting Information).[16] Furthermore, we performed infrared spectrum measurement and the IR data for LSCO-1, LSCO-2, and LSCO-3 is shown in Figure S8 (in the Supporting Information). A vibration band around 664 $cm^{-1}$ represents the $Co^{4+}$–O bond stretching vibration in the $BO_6$ octahedron.[17] The appearance of this vibration band at higher frequencies could be attributed to the interaction between $Co^{4+}$ and O in perovskite $La_{0.5}Sr_{0.5}CoO_{3-\delta}$. The bands around 569 and 588 $cm^{-1}$ are assigned to the two kinds of $Co^{3+}$–O bond bending vibration in the $BO_6$ octahedron.[18] After urea pyrolysis, two bending vibration bands were combined into one band at around 572 $cm^{-1}$ for LSCO-2 and at around 578 $cm^{-1}$ for LSCO-3. This could be attributed to the increase in $CoO_5$ square pyramids owing to the urea pyrolysis reaction. The length of Co–O in the $CoO_5$ square pyramids is between 569 $cm^{-1}$ ($Co_1$–O) and 588 $cm^{-1}$ ($Co_2$–O) in the $CoO_6$ octahedron. Further, the length of Co–O became shorter with the increase in urea content and the Co–O bond bending vibration peak was shifted to a higher frequency but remained below 588 $cm^{-1}$. Therefore, splitting of the peak (220) of LSCO-3 around 69° and the IR spectra implied an increase in $CoO_5$ square pyramids owing to the urea pyrolysis reaction. ESR (electron spin resonance), as a technique to detect paramagnetic lattice defects, is usually used to analyze surface oxygen species at room temperature.[19] The ESR data of the original sample LSCO-1 coincided with other literature data,[20] showing a hump at about 325 mT.[20a] However, after topological reduction and urea pyrolysis, the peak intensity at about 300 mT (*g* 2.21) clearly increased and other small peaks developed at other positions (*g* 3.08 and 2.10), which were attributed to spin interactions of Co ions and various surface oxygen species.[19b,20b,21]

## Surface composition analysis of the perovskite LSCO with different oxygen defects

It is well known that catalytic reactions mainly happen on the surface of solid materials. X-ray photoelectron spectroscopy (XAS), a highly surface-sensitive detection tool, is broadly used to study surface electronic structure. XPS, as a semi-quantitative analysis technique, is usually used to measure the element composition and electronic state of the solid surface. It is very profitable to study structure–activity relationships of materials with the help of XAS and XPS. Modification of the surface electronic structure often causes changes in the surface chemical composition. Surface chemical composition analysis results of LSCO with different oxygen defects are shown in Figure 3(a). Because structure of Co 3p, Co 3s, and La 4d is relatively complicated, it is very difficult to distinguish "surface" components from "lattice" components (XPS data of La 4d and Co 2p are shown in the Supporting Information, Figure S3). Sr 3d and O 1s on the surface of LSCO generally were used to analyze the surface chemical composition and structure.[22] According to previous research, we could separate Sr and O into surface and lattice components, where "surface Sr" located in the high-energy region (approximately 133.4–133.6 eV)[22,23] was considered as $SrCO_3$ or $Sr(OH)_2$; "lattice Sr" located in the low-energy region (approximately 131.6–132.7 eV) was considered as perovskite LSCO; "surface O" located in a higher energy region (approximately 531.1–531.5 eV) was regarded as absorbed oxygen and $SrCO_3$ or $Sr(OH)_2$; and "lattice O" located in a low-energy region (approximately 528.7–529.7 eV) was regarded as perovskite $La_{0.5}Sr_{0.5}CoO_{3-\delta}$. The Sr 3d peak could be fitted and separated into two doublets (Sr $3d_{5/2}$ and $3d_{3/2}$), and Sr $3d_{3/2}$ is about 1.8 eV higher than Sr $3d_{5/2}$, the peak area of Sr $3d_{3/2}$ is about 1.5 times as much as that of Sr $3d_{5/2}$.[23] To directly observe the change in surface chemical composition, we converted the fitting results in Figure 3(a) into a histogram in Figure 3(b), where the integral area ratios were identified as the chemical composition content ratios. We can see that the surface O and Sr content were improved after urea pyrolysis (Figure 3(b)). This is because the topology reduction reaction between LSCO and urea created more oxygen vacancies and the proportion of urea and LSCO had important effect on regulating its oxygen vacancy content. Surface Sr enrichment also could be explained by the increase in oxygen vacancies.[22] In the topology reduction process, $SrCoO_3$ layer enriched on the

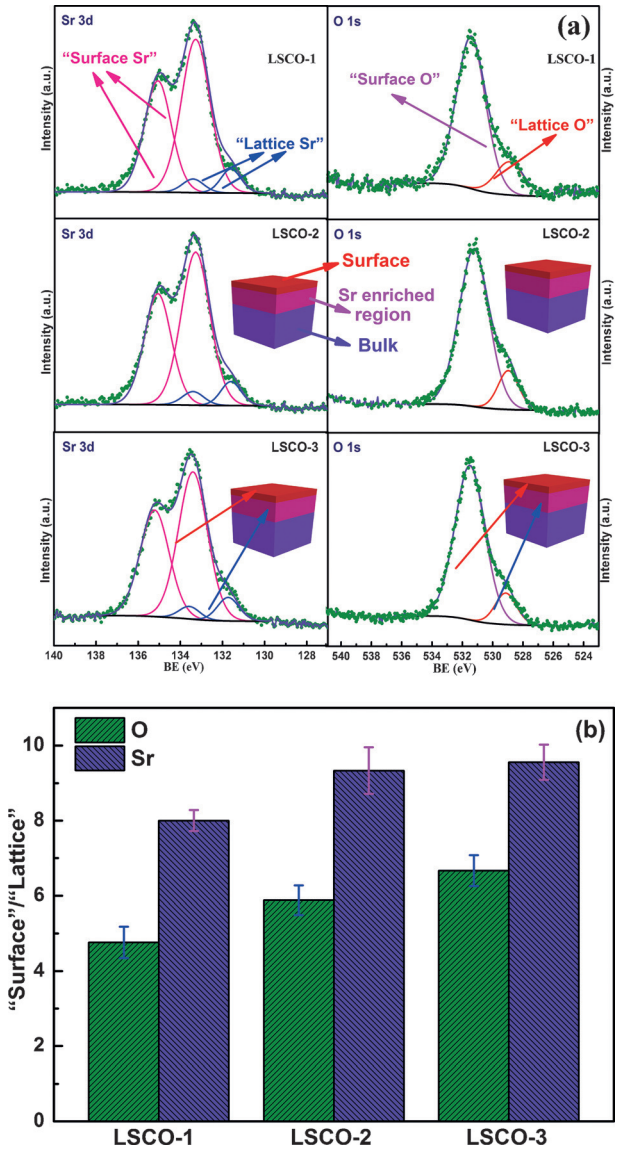


**Figure 3.** (a) XPS data of LSCO with different oxygen defects in the O 1s and Sr 3d regions (green solid circles = measurement; purple line = sum of fits; black line = background; pink line = surface O and Sr; blue line = lattice O and Sr). (b) "Surface" Sr or O (total area)/"lattice" Sr or O (total area) of LSCO-1, LSCO-2, and LSCO-3 by data fitting.

surface of perovskite LSCO lost some oxygen atoms and its surface was reconstructed, where some of the Co–O octahedra transformed into Co–O square pyramids and another part of the $SrCoO_3$ layer transformed into a surface second phase and oxygen vacancies. Hence, we think that urea pyrolysis had positive effect on regulating surface chemical composition and structure.

## The electronic structure of the LSCO with different oxygen defects

To unambiguously comprehend the electronic structure of LSCO with different oxygen defects, X-ray absorption spectroscopy (XAS), as an ideal tool, is used to reflect the electronic state of unoccupied orbitals. The X-ray absorption near edge structure (XANES) O K-edge spectrum normalized from 520 eV to 550 eV, which is related to the metal–O 2p hybridization, is displayed in Figure 4 (a). The pre-edge peak (a) at approximately 526.2 eV, which originates from negative charge transfer Δ, distinctly becomes weaker and weaker with the increase in

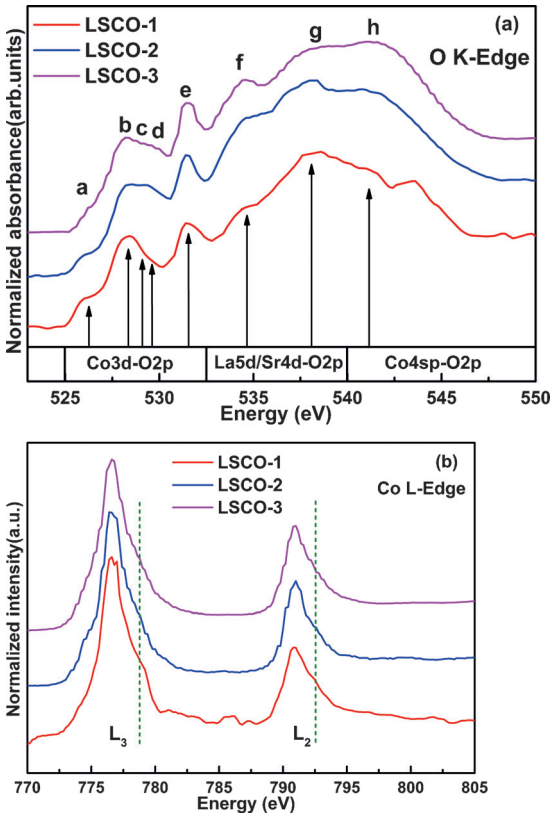


**Figure 4.** (a) The O K-edge XANES of LSCO with different oxygen defects. (b) Evolution of the Co $L_2$-, $L_3$-edges XANES for LSCO-1, LSCO-2, and LSCO-3.

oxygen vacancies.[24] The decrease in $Co^{4+}$ reduces the charge transfer between $Co^{4+}$ and $O^{2-}$. According to a previous report,[25] peaks b, c, and d can be ascribed to the overlapping bands between Co 3d and O 2p; peaks f and g are considered as the result of hybridization between Sr 4d/La 5d and O 2p; peak h is attributed to the overlapping band between Co 4sp and O 2p; and peak e was confirmed to be a superoxide species $O^{2-}$ (or an oxygen gas absorption dip), which in particular exists in the surface region of perovskite $La_{0.5}Sr_{0.5}CoO_{3-\delta}$.[9b,26] From our data in Figure 4 (a), we could clearly see that the area of peak b decreased with the increase in oxygen vacancies compared with peaks c and d. The intensity of peak e (B region) became strong, which was attributed to the square-pyramidal coordination of Co ions after urea pyrolysis. Hence, we could come to the conclusion that urea topology reduction was able to make LSCO gain more oxygen vacancies and its oxygen vacancy concentration could be regulated by designing the proportion of urea and LSCO; introduction of oxygen vacancies narrowed the hybridized orbital between Co 3d and O 2p; more $O_2$ absorbed on the surface and turned into $O^{2-}$ to

generate the superoxide-related peak e in the O K-edge XANES spectrum.

The Co $L_2$, $L_3$ XANES spectrum normalized from 770 eV to 805 eV is presented in Figure 4(b). The Co L-edge has two continuous absorption peaks caused by spin-orbit interactions (Co $2p_{1/2}$ and Co $2p_{3/2}$) and is usually related to the valence state.[25,27] Co $L_2$-edge is on the high-energy side (Co $2p_{1/2} \rightarrow$ Co 3d) and the Co $L_3$-edge is located on the low-energy side (Co $2p_{3/2} \rightarrow$ Co 3d). From Figure 4(b), we could clearly observe that the shoulder of the Co $L_2$-, $L_3$-edge moved towards lower energy with the increase in urea content and their main peak intensity also slightly decreases. This result implies that the average valence of cobalt decreased as a result of urea pyrolysis. Compared with the absorption spectra of the O K-edge and Co L-edge, the Co K-edge absorption spectrum was determined by XANES and EXAFS (extended X-ray absorption fine structure). The XANES spectra represent the transition from Co 1s to Co 4p, but there was also a transition from Co 1s to Co 3d at approximately 15 eV below the main peak owing to hybridization between Co 3d and O 2p. The EXAFS spectra could give us information about the average structure of the materials, and it does not rely on long range order and can give structural information about the neighboring absorbed atoms (coordination number, disorder degree, and bond length, for example). The XANES spectra of LSCO with different urea contents are shown in Figure 5(a). The position of the Co K-edge absorption slightly shifts towards the low energy region with the increase in urea content and its partially enlarged graph is displayed in Figure 5(a). The shift of the LSCO-2 (urea/LSCO 5:1) signal is smaller than that of LSCO-3 owing to the different urea contents, implying that the Co valence in LSCO could be regulated by controlling the topological chemical reaction between urea and LSCO. The Co K-edge $k^3\chi(k)$ oscillation curve of LSCO made by urea pyrolysis is shown in Figure S4 (in the Supporting Information); it displays differences in terms of peak intensity compared with original sample, but the geometrical shape is essentially the same, hinting that their main structure did not undergo a large change. This was further verified by their corresponding Fourier transformed (FT) $k^3\chi(k)$ functions in Figure 5(b), where the first shell at approximately 1.9 Å was Co–O and the second shell at approximately 3.6 Å was Co–La/Sr and Co–Co. For Co–O coordination in the first shell, the peak intensity of LSCO-3 became weak compared with LSCO-1 and LSCO-2, which was attributed to the increase in structure disorder on account of the formation of more oxygen vacancies. Meanwhile, for Co–La/Sr and Co–Co in the second shell, the peak intensity gradually decreased and the peak position visibly shifted to lower bond length with the increase in urea content. Topology reduction by urea pyrolysis brought about formation of $CoO_5$ square pyramids and more octahedral distortion. The fitting data results, such as interatomic distance, Debye–Waller factor, *R*-factor, and inner potential correction, are displayed in the Supporting Information, Table S1, and their fitting data are shown in Figure S4.

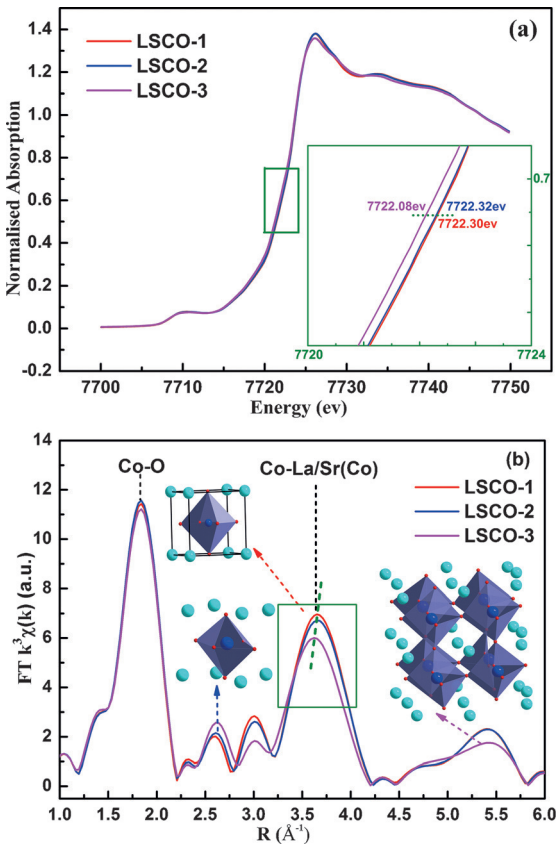


**Figure 5.** (a) The Co K-edge XANES of LSCO with different oxygen defects. (b) The *R*-space Fourier-transformed FT ($k^3\chi(k)$) of Co K-edge EXAFS spectra data of different oxygen defects.

## Correlation between oxygen defects, electronic structure, and catalytic properties

The catalytic properties of perovskite oxides are not only affected by conventional parameters such as metal cations and specific surface area, but also by their structure defects and anion redox chemistry.[8c,28] It is thus very important to understand the correlation between oxygen defects (anion redox chemistry) and catalytic properties. Oxygen activation is the rate-determining step for perovskite catalysts in CO oxidation. The relative location of the valence bond and electronic structure near the Fermi energy are of great importance in the transfer of electrons and holes, which further influences its activity in photocatalytic water splitting. In our work, when the urea content was increased in the topological reduction process, the catalytic properties of regulated perovskite were dramatically enhanced. The specific catalytic activity (CO oxidation and photocatalytic oxygen evolution) is shown in Figure 6(a) and (b). Compared with original sample LSCO-1, the temperature required for 50% conversion decreased by about 20 °C for LSCO-2 and by about 42 °C for LSCO-3 for carbon monoxide oxidation. The water oxidation activity of LSCO-2 was improved by about a factor of two and that of LSCO-3 was increased by about a factor of three. Based on the above experimental data, we could show that the product of urea pyrolysis could react with perovskite LSCO in air at 600 °C, which made LSCO yield more oxygen vacancies and octahedral distortion, and the higher the content of urea was, the more oxygen va-

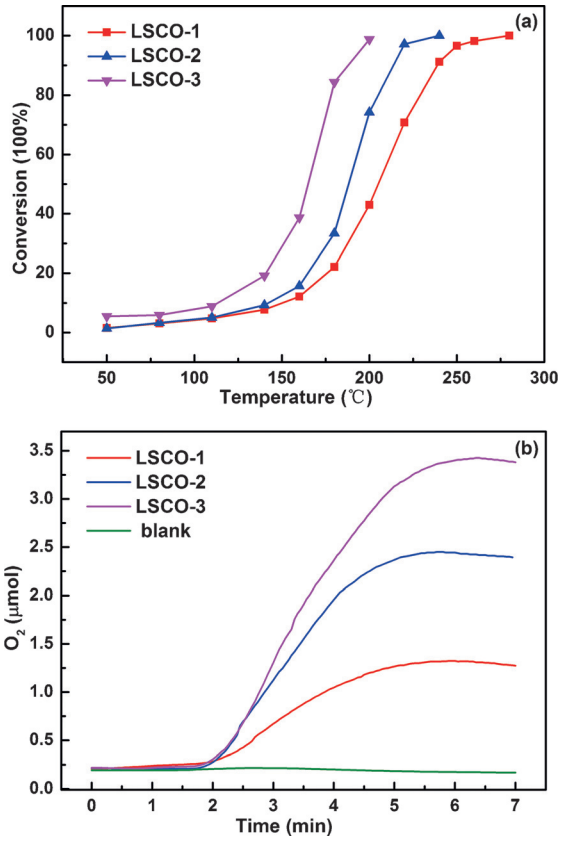


**Figure 6.** (a) CO oxidation activity of LSCO-1, LSCO-2, and LSCO-3. (b) Photocatalytic oxygen evolution with a blank, LSCO-1, LSCO-2, and LSCO-3.

cancies and the higher the degree of distortion of perovskite LSCO was. The valence of Co gradually decreased with the increase in oxygen vacancies from the Co K-edge and Co L-edge absorption spectra. XRD and ESR also showed that the octahedral structure of $CoO_6$ caused distortion, and square pyramids of $CoO_5$ and surface superoxide species clearly increased. The O p-band center that controlled the chemical processes also showed a downshift relative to the Fermi level (valence band XPS spectra of LSCO-1, 2, and 3 are shown in the Supporting Information, Figure S6). With the increase in oxygen vacancies of perovskite LSCO, the degree of hybridization between the O 2p and Co 3d states visibly became weaker, which was extraordinary beneficial to activate oxygen absorbed on the surface of perovskite LSCO. The narrowed electronic state between Co 3d and O 2p not only improved oxygen mobility, but also changed the relative position of Co 3d and O 2p near the Fermi energy, which was likely to give rise to the enhancement of the catalytic activity in CO oxidation and water splitting.

## Conclusion

We designed a simple and cost-effective method to engineer oxygen defects of perovskite oxides and could well regulate the oxygen defect concentration by adjusting the proportion of perovskite LSCO and urea. By carrying out surface-sensitive XAS, used to characterize the electronic structure, we found that oxygen defects (anion redox chemistry) also play a key role in the covalent part of the TM–O bond and O p-band center. Specifically, we observed that introduction of more oxygen vacancies narrowed the overlap between the Co 3d state and O 2p state and also increased the absorbed oxygen on the surface of perovskite LSCO, resulting in improvement of oxygen mobility and optimization of the relative location for Co 3d, O 2p, and the valence band near the Fermi level, which is beneficial for improving the catalytic activity in carbon monoxide oxidation and photocatalytic water splitting. The relationship between oxygen defects, electronic structure, and catalytic properties such as carbon monoxide oxidation and photocatalytic water splitting activity of the perovskite $La_{0.5}Sr_{0.5}CoO_{3-\delta}$ furthermore showed that an isolated comprehension of which transition metal cations act as redox partner is insufficient. These important insights into defect engineering and effect of anion redox chemistry on the electronic structure and catalytic property provide a new avenue to design highly efficient catalysts.

## Experimental Section

### Materials synthesis

$La_{0.5}Sr_{0.5}CoO_{3-\delta}$ catalysts were synthesized through a sol-gel method. $La(NO_3)_3{\cdot}6H_2O$, $Sr(NO_3)_2$, and $Co(NO_3)_2{\cdot}6H_2O$ in a stoichiometric ratio were dissolved in distilled water (10 mL).[29] Citric acid monohydrate was added to the mixture in 12% excess to ensure complete complexation of the metal ions. An appropriate amount of polyvinyl alcohol was added to the solution to achieve the desired viscosity. The solution was stirred at room temperature for 2 h. The resulting solution was then heated to 80 °C with continuous stirring until a viscous and transparent gel formed. The gel was subsequently dried overnight at 240 °C. The resulting fluffy spongy LSCO precursor was crushed and then was calcined in air at 950 °C for 10 h at a heating rate of 3 °C $min^{-1}$.

### Defect regulation of materials

The catalysts were mixed with urea at the desired ratio (catalyst/urea 5:1 or 1:2). Then, the mixture was crushed adequately and calcined for 1 h at 550–650 °C in air with 5 °C $min^{-1}$ heating rate.

### Materials characterization

The catalysts with different oxygen vacancy concentrations were characterized by X-ray powder diffraction (XRD), which was collected with an Ultima IV diffractometer with $Cu_{K\alpha}$ radiation ($\lambda$ 0.15418 nm) at 40 kV and 30 mA at room temperature by step scanning in an angle range of 20°–80°. X-ray photoelectron spectroscopy (XPS) was recorded with a Thermo ESCALab 250 analyzer operating at constant analyzer energy mode and using monochromatic $Al_{K\alpha}$ radiation (1486.6 eV). The binding energy of the acquired spectra was referenced to the C 1s line at 284.6 eV. A thermobalance with a differential thermal analysis attachment (TGA Q500) was used for the TG-DTA study. In this study, these samples were analyzed at a heating rate of 10 °C $min^{-1}$ with a flow rate of 50 mL $min^{-1}$ in air at 1 bar and the sample mass was 8.0 mg. ESR spectra were obtained with a JES-FA200 ESR spectrometer at room temperature. High-energy X-ray absorption spectra (XAS) of the Co K-edge were measured at the beamline BL14W1 (Shanghai Synchrotron Radiation Facility). XAS spectra (EXAFS and XANES re-

gions) were carried out at room temperature in transmission mode, by using self-supported wafers of the perovskite oxide samples with LiF diluents, monochromatized by utilizing a Si (111) channel-cut monochromator. A standard Co foil was introduced to realize energy calibration. Typical XAS spectra of Co K-edge were recorded from 7500 eV to 8500 eV, with a variable step energy value, with a minimum 0.2 eV step across the XANES region. The EXAFS oscillations were Fourier transformed in the range 2.0–12.0 $Å^{-1}$. These experimental data were analyzed and fitted by using the software package IFEFFIT. The coordination numbers, interatomic distances, Debye–Waller factor, and inner potential correction were used as variable parameters for the fitting procedures. The Co L-edge and O K-edge X-ray absorption near-edge (XANES) spectra were measured in the total electron yield (TEY) mode by collecting sample drain current under a vacuum better than $5\times10^{-8}$ Pa, which was carried out at the BL12B-a beamline of the National Synchrotron Radiation Laboratory (NSRL) in China. The beam from a bending magnet was monochromatized with a varied line-spacing plane grating and refocused by a toroidal mirror. The oxygen-deficient content $\delta$ value was deduced by calculating the cobalt oxidation state by chemical titration. These samples (LSCO-1, LSCO-2, and LSCO-3) weighed about 15 mg and were dissolved in 30 mL 3 M HCl, where KI (0.14 g) and starch (10 mg) was added. $I^-$ was easily oxidized into $I_2$ owing to the strong oxidizing property of $Co^{3+}$ and $Co^{4+}$ in the acidic environment. Then, $Na_2S_2O_3$ (0.015 mol $L^{-1}$) was used to calibrate the content of $I_2$. Further, we could calculate the $\delta$ value by electron transfer balance. The titration experiment was repeated three times for every sample. Infrared spectroscopy (FTIR) was recorded with an IFS-66V/S infrared spectrum radiometer. These samples were pressed as pellets with the weight ratio of sample to KBr of 1:120. The instrument measurement range is from 400 $cm^{-1}$ to 2000 $cm^{-1}$. The instrument resolution was set at 4 $cm^{-1}$ during the measurements.

### CO oxidation and water splitting

The activities of the catalysts were tested in a fixed-bed quartz reactor (inner diameter of 5 mm) using catalyst (50 mg, 40–60 mesh). The feed gas mixture contained 1% CO, 20% $O_2$, and the carrier gas was Ar. The total flow rate of the feed gas was 50 $cm^3 min^{-1}$. The concentrations of the CO were analyzed by gas chromatography (Agilent, GC6890N) equipped with a TCD. The conversion rate was obtained by calculating the concentrations of CO at different temperatures.

Photocatalytic water oxidation was performed in a quartz vessel fitted with a water jacket for maintaining the temperature at $19\pm0.5\,^{\circ}C$. Catalyst (5 mg), $[Ru(bpy)_3]Cl_2\cdot6H_2O$ (0.5 mM; bpy = bipyridine), $Na_2S_2O_8$ (10 mM), sodium fluorosilicate (20 mL), and sodium bicarbonate buffer solution (pH 7.0) were used in this experiment. All profiles were corrected accordingly and the mixture was purged with $N_2$ to get zero oxygen detection by a Clark electrode. The reaction vessel was irradiated with a 300 W Xe lamp fitted with a 420 nm cut-off filter and evolved oxygen was detected by a Clark electrode. The measurements were recorded for 7 min owing to consumption of sacrificial electron acceptor or the decomposition of $[Ru(bpy)_3]^{2+}$ as already described by others.[30]

## Acknowledgments

This work was supported by the National Natural Science Foundation of China (NSFC Grants 21671076, 21427802, and 21131002). The authors thank the beamline BL14W1 (Shanghai Synchrotron Radiation Facility) for providing beam time. The authors thank the NSRL beamline BL12B-a (National Synchrotron Radiation Laboratory) for providing beam time.

**Keywords:** catalytic properties · cobalt · electronic structure · oxygen vacancies · urea pyrolysis

[1] a) W. Liu, M. Flytzanistephanopoulos, *J. Catal.* **1995**, *153*, 317–332; b) A. Dangwal Pandey, C. Jia, W. Schmidt, M. Leoni, M. Schwickardi, F. Schüth, C. Weidenthaler, *J. Phys. Chem. C* **2012**, *116*, 19405–19412.
[2] W. C. Chueh, C. Falter, M. Abbott, D. Scipio, P. Furler, S. M. Haile, A. Steinfeld, *Science* **2010**, *330*, 1797–1801.
[3] M. W. Kanan, D. G. Nocera, *Science* **2008**, *321*, 1072–1075.
[4] Y. Sun, Q. Liu, S. Gao, H. Cheng, F. Lei, Z. Sun, Y. Jiang, H. Su, S. Wei, Y. Xie, *Nat. Commun.* **2013**, *4*, 2899.
[5] J. Li, U. G. Singh, T. D. Schladt, J. K. Stalick, S. L. Scott, R. Seshadri, *Chem. Mater.* **2008**, *20*, 6567–6576.
[6] a) Y. Sun, S. Gao, F. Lei, C. Xiao, Y. Xie, *Acc. Chem. Res.* **2015**, *48*, 3–12; b) H. Wang, J. Zhang, X. Hang, X. Zhang, J. Xie, B. Pan, Y. Xie, *Angew. Chem. Int. Ed.* **2015**, *54*, 1195–1199; *Angew. Chem.* **2015**, *127*, 1211–1215; c) R. P. Haggerty, R. Seshadri, *J. Phys. Condens. Matter* **2004**, *16*, 6477–6484.
[7] K. Huang, X. Chu, L. Yuan, W. Feng, X. Wu, X. Wang, S. Feng, *Chem. Commun.* **2014**, *50*, 9200–9203.
[8] a) E. Bucher, W. Sitte, *J. Electroceram.* **2004**, *13*, 779–784; b) M. Søgaard, P. V. Hendriksen, M. Mogensen, *J. Solid State Chem.* **2007**, *180*, 1489–1503; c) S. Royer, D. Duprez, *ChemCatChem* **2011**, *3*, 24–65.
[9] a) J. T. Mefford, W. G. Hardin, S. Dai, K. P. Johnston, K. J. Stevenson, *Nat. Mater.* **2014**, *13*, 726–732; b) D. N. Mueller, M. L. Machala, H. Bluhm, W. C. Chueh, *Nat. Commun.* **2015**, *6*, 6097.
[10] S. Royer, D. Duprez, F. Can, X. Courtois, C. Batiot-Dupeyrat, S. Laassiri, H. Alamdari, *Chem. Rev.* **2014**, *114*, 10292–10368.
[11] a) Y. Orikasa, T. Ina, T. Nakao, A. Mineshige, K. Amezawa, M. Oishi, H. Arai, Z. Ogumi, Y. Uchimoto, *Phys. Chem. Chem. Phys.* **2011**, *13*, 16637–16643; b) D. N. Mueller, R. A. De Souza, J. Brendt, D. Samuelis, M. Martin, *J. Mater. Chem.* **2009**, *19*, 1960–1963; c) A. Grimaud, K. J. May, C. E. Carlton, Y.-L. Lee, M. Risch, W. T. Hong, J. Zhou, Y. Shao-Horn, *Nat. Commun.* **2013**, *4*, 2439; d) J. Suntivich, H. A. Gasteiger, N. Yabuuchi, H. Nakanishi, J. B. Goodenough, Y. Shao-Horn, *Nat. Chem.* **2011**, *3*, 546–550.
[12] a) J. Du, T. Zhang, F. Cheng, W. Chu, Z. Wu, J. Chen, *Inorg. Chem.* **2014**, *53*, 9106–9114; b) K. R. Poeppelmeier, M. E. Leonowicz, J. M. Longo, *J. Solid State Chem.* **1982**, *44*, 89–98.
[13] Y. Qiu, L. Gao, *Mater. Res. Bull.* **2005**, *40*, 794–799.
[14] P. M. Schaber, J. Colson, S. Higgins, D. Thielen, B. Anspach, J. Brauer, *Thermochim. Acta* **2004**, *424*, 131–142.
[15] a) S. Sengodan, S. Choi, A. Jun, T. H. Shin, Y.-W. Ju, H. Y. Jeong, J. Shin, J. T. S. Irvine, G. Kim, *Nat. Mater.* **2014**, *14*, 205–209; b) Z. Lin, G. Waller, Y. Liu, M. Liu, C.-P. Wong, *Adv. Energy Mater.* **2012**, *2*, 884–888.
[16] a) Y. Zhu, W. Zhou, J. Yu, Y. Chen, M. Liu, Z. Shao, *Chem. Mater.* **2016**, *28*, 1691–1697; b) N. Dasgupta, R. Krishnamoorthy, K. T. Jacob, *J. Mater. Sci. Eng. B* **2002**, *90*, 278–286.
[17] D. Berger, V. Fruth, I. Jitaru, J. Schoonman, *Mater. Lett.* **2004**, *58*, 2418–2422.
[18] H. Wang, Z. Zhao, P. Liang, C. Xu, A. Duan, G. Jiang, J. Xu, J. Liu, *Catal. Lett.* **2008**, *124*, 91–99.
[19] a) T. Kolodiazhnyi, G. Annino, A. Younker, P. Malysz, P. Mascher, H. Haneda, *J. Eur. Ceram. Soc.* **2006**, *26*, 1921–1924; b) J. N. Kuhn, P. H. Matter, J.-M. M. Millet, R. B. Watson, U. S. Ozkan, *J. Phys. Chem. C* **2008**, *112*, 12468–12476.
[20] a) T. L. Phan, L. V. Bau, N. V. Khiem, N. X. Phuc, S. C. Yu, *Phys. Status Solidi B* **2005**, *242*, 1522–1527; b) T.-L. Phan, S.-C. Yu, N. Van Khiem, M.-H. Phan, J. R. Rhee, N. X. Phuc, *J. Appl. Phys.* **2005**, *97*, 10A508.
[21] R. A. Eichel, *Phys. Chem. Chem. Phys.* **2011**, *13*, 368–384.
[22] E. J. Crumlin, E. Mutoro, Z. Liu, M. E. Grass, M. D. Biegalski, Y.-L. Lee, D. Morgan, H. M. Christen, H. Bluhm, Y. Shao-Horn, *Energy Environ. Sci.* **2012**, *5*, 6081.
[23] a) R. P. Vasquez, *J. Electron Spectrosc. Relat. Phenom.* **1991**, *56*, 217–240; b) P. A. W. van der Heide, *Surf. Interface Anal.* **2002**, *33*, 414–425.

[24] a) R. H. Potze, G. A. Sawatzky, M. Abbate, *Phys. Rev. B* **1995**, *51*, 11501 – 11506; b) M. Medarde, A. Fontaine, J. L. García-Muñoz, J. Rodríguez-Carvajal, M. de Santis, M. Sacchi, G. Rossi, P. Lacorre, *Phys. Rev. B* **1992**, *46*, 14975 – 14984.
[25] L. Karvonen, M. Valkeapää, R.-S. Liu, J.-M. Chen, H. Yamauchi, M. Karppinen, *Chem. Mater.* **2010**, *22*, 70 – 76.
[26] M. Imamura, N. Matsubayashi, H. Shimada, *J. Phys. Chem. B* **2000**, *104*, 7348 – 7353.
[27] Y. Orikasa, T. Ina, T. Nakao, A. Mineshige, K. Amezawa, M. Oishi, H. Arai, Z. Ogumi, Y. Uchimoto, *J. Phys. Chem. C* **2011**, *115*, 16433 – 16438.
[28] M. Peña, J. Fierro, *Chem. Rev.* **2001**, *101*, 1981 – 2018.
[29] H. Wang, Z. Zhao, C. Xu, J. Liu, Z. Lu, *Chin. Sci. Bull.* **2005**, *50*, 1440 – 1444.
[30] a) B. Deibert, J. Zhang, P. Smith, K. Chapman, S. Rangan, D. Banerjee, K. Tan, H. Wang, N. Pasquale, F. Chen, *Chem. Eur. J.* **2015**, *21*, 14218-14228; b) D. Robinson, Y. Go, M. Mui, G. Gardner, Z. Zhang, D. Mastrogiovanni, E. Garfunkel, J. Li, M. Greenblatt, G. Dismukes, *J. Am. Chem. Soc.***2013**, *135*, 3494-3501.

Manuscript received: August 26, 2016
Accepted Article published: November 2, 2016
Final Article published: December 16, 2016